JOURNAL OF AIRCRAFT
Vol. 45, No. 5, September–October 2008

Transonic Limit Cycle Flutter of High-Aspect-Ratio Swept Wings

Oddvar O. Bendiksen*
University of California, Los Angeles, Los Angeles, California 90095-1597

DOI: 10.2514/1.29547

This paper is motivated by the observed transonic limit cycle flutter of a high-aspect-ratio swept wing tested at DLR, German Aerospace Center in Göttingen. We show that the aeroelastic mechanism responsible for the limit cycle flutter behavior can be explained in terms of the structural washout effect, which is strongly stabilizing at transonic Mach numbers. This limits the energy transfer rate to the wing, resulting in a limit cycle flutter mode in which bending and torsion are almost perfectly in phase, and the streamwise wing-section motion resembles a single-degree-of-freedom torsion mode with an axis of rotation forward of the leading edge. For swept wings, the apparent pitching motion of the wing sections arises naturally through the structural washout and is present in the first bending mode that enters limit cycle flutter. The aeroelastic washout effect may produce counterintuitive results, and increasing the dynamic pressure may actually be stabilizing. In such a case, decreasing the dynamic pressure would increase the limit cycle amplitude, and high-altitude transonic flutter becomes a real possibility. The results demonstrate the importance of using a nonlinear structural model in these calculations. If a linear structural model is used, the critical dynamic pressure at limit cycle flutter onset is overpredicted by a factor of nearly 3, and the predicted flutter mode is at a frequency much higher than was observed during wind-tunnel tests.

Nomenclature

A = aspect ratio
A_e = element area
C_p = pressure coefficient $[(p - p_\infty)/\frac{1}{2}\rho_\infty U_\infty^2]$
c = airfoil or wing chord, $2b$
E = Young's modulus
E_{tot} = total energy (structure) $(T + U)$
G = shear modulus
h = plate thickness
k = reduced frequency $(\omega b/U_\infty)$
M = Mach number
m = mass per unit span
p = pressure
T = kinetic energy
t = time
U = strain energy
$\mathbf{U}$ = mesh velocity vector with components U_i
U_∞ = freestream velocity at upstream infinity
u, v, w = plate or wing displacements in the x, y, and z directions
$\mathbf{u}$ = fluid velocity vector with components u_i
α = angle of attack
β_x, β_y = rotations of normals in the x–z and y–z planes
γ = ratio of specific heats
$\{\gamma\}$ = shear strains
$\Delta u, \Delta v$ = wing in-plane displacements in the chordwise and spanwise directions, relative to the steady aeroelastic equilibrium position of the wing
$\{\varepsilon_m\}$ = membrane strains
$\eta = y/y_{\text{tip}}$ = relative span location
$\{\varepsilon_n\}$ = nonlinear strains
$\{\kappa\}$ = plate element curvatures
Λ = sweep angle
λ = taper ratio
ν = Poisson's ratio
ρ = density
τ = nondimensional time $(\omega_{1T}t/2\pi)$
ω = circular frequency
ω_{1T} = frequency of the first torsion mode in vacuum

Subscripts

a = air
e = element
LE, TE = leading and trailing edges, respectively
∞ = conditions at upstream infinity

I. Introduction

SWEPT wings of high aspect ratio are generally prone to the more dangerous types of aeroelastic instabilities, such as primary bending-torsion flutter, in which energy is extracted from the airstream at a sufficient rate to produce rapidly increasing flutter amplitudes [1]. In the transonic region, moving shocks on the wing surface introduce strong aerodynamic nonlinearities, which tend to limit the rate of energy transfer to the wing, resulting in limit cycle flutter.[†] Aerodynamic nonlinearities from shock dynamics play a fundamental role in transonic control surface flutter as well [2,3]. Structural nonlinearities can also result in LCO-type flutter at subsonic and supersonic Mach numbers, but the nature of the flutter instability is usually very different in transonic flow compared with subsonic or supersonic flow [4].

Transonic limit cycle flutter and other LCO phenomena have been observed in a wide variety of aircraft during flight [2], in wind-tunnel tests [5–11], and in time-marching flutter calculations [4,12–20]. For limit cycle flutter to occur, there must exist a mechanism for limiting the energy flow from the fluid to the structure, and the cutoff must be sufficiently rapid to prevent the destructive (exponential) amplitude growth normally associated with bending-torsion flutter. In the absence of separation, the dominant energy-limiting mechanism appears to be a transition from Tijdeman type A to type B shock motion, which provides a rapid throttling of the aerodynamic work

---

Presented as Paper 1635 at the 47th AIAA/ASME/ASCE/AHS/ASC Structures, Structural Dynamics and Materials Conference, Newport, RI, 1–4 May 2006; received 31 December 2006; revision received 26 February 2008; accepted for publication 26 February 2008.

*Professor, Department of Mechanical and Aerospace Engineering. Associate Fellow AIAA.

[†] Also referred to as limit cycle oscillations (LCO) in some contexts.

done on the wing [20]. Intermittent trailing-edge separation caused by shock/boundary-layer interactions is believed to have a very similar effect [6] and would affect the transition of type A to B as well. Additional discussions of the influence of viscous effects in limiting the energy flow in transonic LCO-type flutter can be found in [21].

The present paper is motivated by the observed limit cycle flutter on a high-aspect-ratio swept wing of a representative transport aircraft [8] (Fig. 1), hereafter referred to as the Göttingen wing. Although the flutter data in [8] are somewhat sketchy, the results show that the wing encounters limit cycle flutter at a Mach number of 0.865, which is uncomfortably close to typical cruise Mach numbers. The flutter amplitude was not stated but can be estimated from Fig. 1b as approximately 12% of the tip chord, at the tip trailing edge, and the flutter mode resembles the first bending mode. Because the limit cycle flutter occurred on a clean wing mounted to the wind-tunnel wall, it appears different from the more common LCOs that occur on fighter wings (e.g., the F-16). In the latter case, tip missiles and/or stores play a fundamental role, and the flutter mode is antisymmetric with respect to the longitudinal plane of symmetry. Also, because the LCO was encountered at an angle of attack and lift coefficient close to design, it cannot be classified as stall flutter, nor is it evident from the experimental data that trailing-edge separation played a fundamental role in the observed limit cycle flutter, as was believed to be the case in the LCOs reported in [9,11].

It is a main conjecture of the present paper that the aeroelastic mechanism responsible for the observed limit cycle flutter of the Göttingen wing is fundamentally different from the corresponding mechanism(s) responsible for the LCO-type flutter of low-aspect-ratio wings, as observed on the F-16 aircraft [22], for example. In the case of a high-aspect-ratio swept wing, the structural washout effect from aeroelastic deformations plays a fundamental role in throttling the energy flow from the airstream to the wing, resulting in limit cycle flutter. In the present paper, we show that this mechanism is strong enough to explain the low-amplitude LCOs observed in the Göttingen wing tests, even in the absence of flow separation. Furthermore, because aeroelastic washout is present in *all* high-aspect-ratio swept wings, the results in this paper should be of interest to flutter engineers and designers of transonic wings and might add further insight to the results reported in [9–11].

In the case of flexible high-aspect-ratio wings, sweep has a profound effect on the flutter mode in the nonlinear transonic region close to the transonic dip. For aft sweep in the 30–40-deg range typical of large subsonic/transonic aircraft, the resulting structural washout effect is strongly stabilizing at transonic Mach numbers, more so than would be predicted by linear theories. The main reason appears to be that the aeroelastic "untwist" unloads the critical tip region of the wing, changing the 3-D shock structure on the outboard region in a stabilizing direction as far as flutter is concerned. The resulting transonic limit cycle flutter mode has bending and torsion almost perfectly in phase (at any given span location), and the 2-D streamwise wing-section motion resembles a single-degree-of-freedom (SDOF) torsion mode with an axis of rotation forward of the leading edge. In the swept-wing case, the apparent pitching motion of the streamwise wing sections arises naturally through the structural washout effect and is present in the first bending mode that enters LCO flutter (Fig. 1b).

The so-called *structural washout effect* is illustrated in more detail in Fig. 2 and arises from the fact that streamwise and chordwise segments undergo different rotations about the unswept *y* axis when the wing bends. Because the structural washout reduces the effective angle of attack of streamwise chord sections, it reduces the aerodynamic twisting moment about the elastic axis and is consequently very beneficial from a divergence standpoint. The effect on flutter stability is less clear, but linear theory again predicts a beneficial effect of aft sweep. In the nonlinear transonic region, the results of this paper suggest that aft sweep should be stabilizing for flexible high-aspect-ratio wings,[‡] and the stabilizing effect is a nonlinear function of wing amplitude. As the wing bends, it unloads the outboard tip region, reducing the shock strength and moving the part-chord shocks forward, toward the leading edge. The weaker and more forward shocks lead to an earlier transition (at lower amplitudes) from Tijdeman type A to type B shock motion, which decreases the rate of the aerodynamic work by the air on the wing [20]. The result is a limit cycle flutter mode that persists over a relatively wide range of dynamic pressures and densities (altitudes). In this context, it should be noted that other researchers have proposed different energy-limiting mechanisms for explaining LCO-type flutter; however, the important role played by the structural washout in transonic limit cycle flutter has not been considered in previous studies.

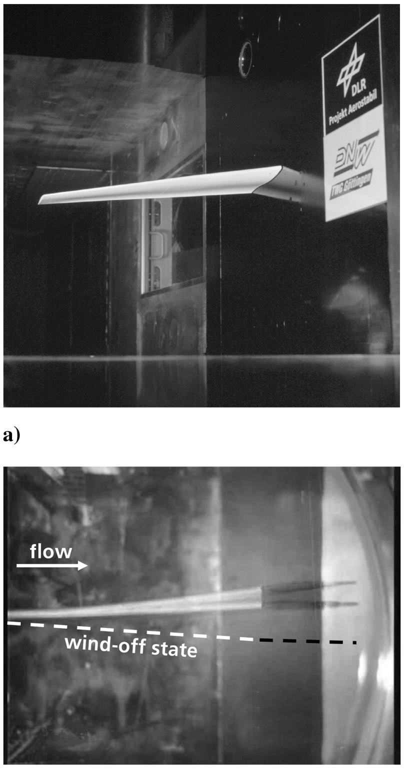

a)

b)

Fig. 1 Göttingen wing a) mounted in the wind tunnel and b) observed limit cycle flutter during wind-tunnel tests (adapted from [8]).

The present investigation is based on an inviscid flow model and therefore cannot capture the important interactions that occur between the shocks and the boundary layer during limit cycle flutter. We still believe that the results obtained in this paper are of practical interest in transonic limit cycle flutter calculations for high-aspect-ratio wings operating at the *low* angles of attack typical of design conditions. The results also show that nonlinear structural effects are important and should be included in LCO calculations for this class of wings. It appears that the present analysis correctly identifies the low-amplitude LCO mode observed in wind-tunnel tests of the Göttingen wing. This suggests that viscous effects, such as shock/boundary-layer interactions, may not be playing a fundamental role in *causing* the observed LCO-type flutter instability in this case, but rather enter the problem as another mechanism through which the energy flow from the fluid to the structure is further reduced as the LCO amplitudes increase. If this conjecture is correct, the calculated limit cycle amplitudes using the Navier–Stokes equations should be smaller than the corresponding amplitudes calculated using the Euler equations. In transonic limit cycle flutter cases in which the angle of attack and lift coefficient are significantly higher, however, this argument cannot be made and a viscous flow model may become essential to capture the instability mechanism itself.

[‡] After this paper was submitted, additional results obtained for unswept wings suggest that in some cases, the effect of sweep may be destabilizing from a transonic flutter boundary standpoint [23]. However, the important beneficial effects from structural washout in limiting the flutter amplitudes remain, resulting in LCO-type flutter rather than strong flutter.

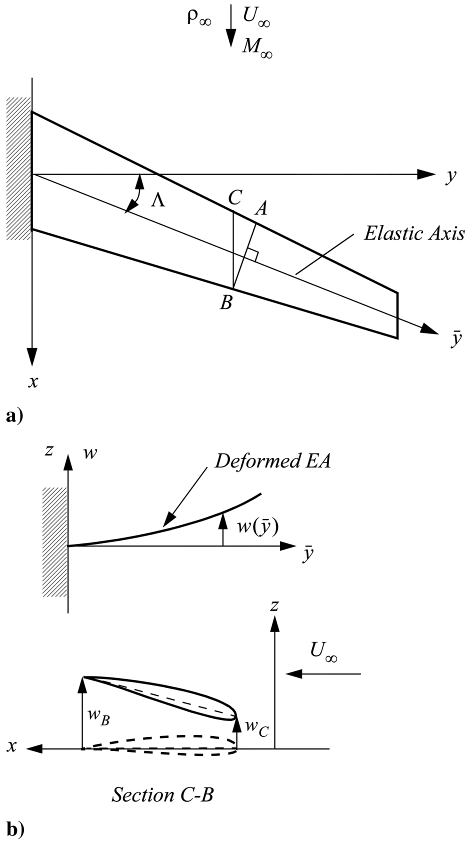

Fig. 2 Elastic deformations of a swept wing: a) chordwise segment *A–B* vs streamwise segment *C–B* and b) structural washout effect (reduction of angle of attack of streamwise segment *C–B*, because $w_C < w_B$).

II. Computational Approach

The calculations in the present paper are based on a nonlinear time-accurate finite element formulation, applicable to a general class of aeroelastic problems with large deformations and formulated such that the aeroelastic response can be determined by an explicit time-marching scheme. The approach is a generalization of the direct Eulerian–Lagrangian computational scheme introduced in [14]. Both structural and aerodynamic nonlinearities are modeled, and the formulation makes use of individual element-fixed local Lagrangian coordinate systems in addition to a global Eulerian system. Calculations are done at the finite element level, both in the fluid and structural domains, and the fluid–structure system is time-marched as a single dynamical system using a multistage Runge–Kutta scheme. The exact nonlinear boundary condition at the wing surface is satisfied using the actual deformation of the wing, as defined by the finite element shape functions and the local element coordinates. The generalized forces associated with the in-plane and out-of-plane degrees of freedom are calculated in a local Lagrangian (element) coordinate system that fully accounts for large rigid-body translations and rotations, thus removing the amplitude restriction inherent in the von Kármán plate theory. Further details can be found in [24].

A. Nonlinear Structural Model

The structural model is essentially that of [24], but modified as needed to perform the calculations discussed in Sec. III. This model is of a construction that has been used extensively in wind-tunnel tests and it consists of a thin aluminum plate of the same planform as the wing, which is then covered by balsa wood or lightweight plastic foam to form the desired airfoil shape. Triangular plate elements based on the Mindlin–Reissner theory are used to model the wing structure. Figure 3 shows a typical triangular structural finite element in its undeformed and deformed configurations. The xyz coordinate system is a fixed Eulerian system with respect to which the response of the wing structure is expressed, and the $x'y'z'$ system is an element-fixed local coordinate system that moves with the corresponding element at all times. It is Lagrangian in the sense that the axes are fixed to three points in the structural element. The elastic deformations of each element are defined relative to these local systems.

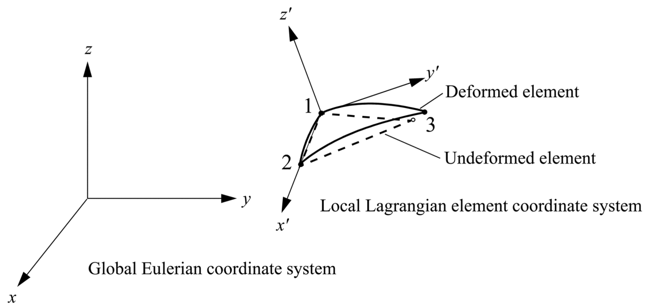

Fig. 3 Eulerian and Lagrangian coordinate systems used in the direct Eulerian–Lagrangian computational scheme.

At any given time step, the three corner nodes of the triangular finite element form a plane. The z' axis is defined orthogonal to this plane by taking the cross product of the two planar vectors from the origin (node 1) to the remaining two nodes. The x' axis is aligned along nodes 1 and 2, and the y'-axis orientation is determined such that a right-handed coordinate system is formed (see Fig. 3). Any vector (displacements, forces, etc.) can then be expressed in either the local element coordinates or the global system coordinates, and the two representations are related through an orthogonal transformation involving the direction cosines between the corresponding coordinate axes.

The nonlinear structural model makes use of three basic finite elements to model the in-plane, out-of-plane, and nonlinear behaviors, as shown in Fig. 4. First, a Mindlin–Reissner discrete shear triangle (DST) is used to model the out-of-plane bending and the transverse shear behavior. This element is based on the formulation in [25] and is extended to dynamics problems in [26]. It is free of shear locking and converges to the discrete Kirchhoff triangular element when the shear deformations become negligible. Second, a constant-strain triangle (CST) models the in-plane behavior and its shape functions are used in connection with the corresponding shape functions of the DST element to create the stress-stiffening matrix in local element coordinates. Third, a stress-stiffening matrix provides the in-plane and out-of plane coupling effects. It is based on the von Kármán plate theory, which assumes that the nonlinear strain components arising from the in-plane displacement gradients are small compared with the corresponding terms arising from the transverse displacement gradients and may therefore be neglected. This is a reasonable assumption in the present calculations, because the deformations relative to the local Lagrangian element coordinate systems are always small if linearly elastic behavior is assumed.

The total strain energy of an element can be expressed as a sum of the component strain energies as

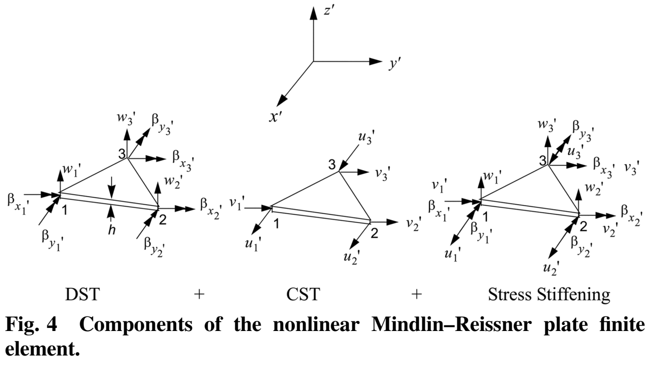

Fig. 4 Components of the nonlinear Mindlin–Reissner plate finite element.

$$U^e_{\text{total}} = U_m + U_b + U_S + U_{N1} + U_{N2} \tag{1}$$

where U_m, U_b, and U_s are the quadratic-order strain energies representing the membrane stretching (CST), out-of-plane bending, and shear (DST), respectively:

$$U_m = \frac{1}{2}\int_{A_e} \{\varepsilon_m\}^T [D_m] \{\varepsilon_m\}\,\mathrm{d}A \qquad U_b = \frac{1}{2}\int_{A_e} \{\kappa\}^T [D_b] \{\kappa\}\,\mathrm{d}A$$
$$U_S = \frac{1}{2}\int_{A_e} \{\gamma\}^T [D_S] \{\gamma\}\,\mathrm{d}A \tag{2}$$

where A_e is the element area and

$$[D] = \frac{E}{1-\nu^2}\begin{bmatrix} 1 & \nu & 0 \\ \nu & 1 & 0 \\ 0 & 0 & \frac{1-\nu}{2} \end{bmatrix} \tag{3}$$

$$[D_m] = h[D] \qquad [D_b] = \frac{h^3}{12}[D] \tag{4}$$

$$[D_S] = kGh\begin{bmatrix} 1 & 0 \\ 0 & 1 \end{bmatrix} = \frac{kEh}{2(1+\nu)}\begin{bmatrix} 1 & 0 \\ 0 & 1 \end{bmatrix} \tag{5}$$

In Eq. (5), k is the shear correction factor ($\frac{5}{6}$ for isotropic plates). The cubic-order strain energy U_{N1} represents the nonlinear coupling of the in-plane and out-of-plane motion, and the quartic-order strain energy U_{N2} represents the nonlinear coupling effect of slope due to large deflections:

$$U_{N1} = \int_{A_e} \{\varepsilon_m\}^T [D_m] \{\varepsilon_n\}\,\mathrm{d}A$$
$$U_{N2} = \int_{A_e} \{\varepsilon_n\}^T [D_m] \{\varepsilon_n\}\,\mathrm{d}A \tag{6}$$

To obtain an element free of shear locking, the equilibrium equations are used to solve for the transverse shear strains, with the help of the constitutive equations. The stiffness matrix is then formulated using quadratic interpolation functions for the rotation fields. The stiffness matrix for the in-plane CST is based on linear interpolation functions, and the development is well-known and available in standard finite element texts.

The element stiffness matrix of the nonlinear model can be obtained from the principle of stationary potential energy, using the strain-energy relations. To calculate the nonlinear coupling partition, the values of the nodal degrees of freedom are required at the current time step. The structure of the element stiffness matrix is as follows:

$$[K_e]_{15\times 15} = \begin{bmatrix} [\mathrm{DST}] & [\mathrm{NLC}] \\ [\mathrm{NLC}]^T & [\mathrm{CST}] \end{bmatrix}$$
$$[\mathrm{DST}]_{9\times 9} = \text{out-of-plane partition}$$
$$[\mathrm{CST}]_{6\times 6} = \text{in-plane partition} \tag{7}$$
$$[\mathrm{NLC}]_{9\times 6} = \text{nonlinear coupling partition}$$

The deformed unit vectors are updated at each time step by the incremental rotations in the global x and y directions, using finite rotation relations. The cubic interpolation functions derived in [26] are used as a basis for deriving the consistent mass matrix and the generalized aerodynamic loads. All integrals are evaluated using Gaussian integration in natural (triangular) coordinates (for further details, see [24]).

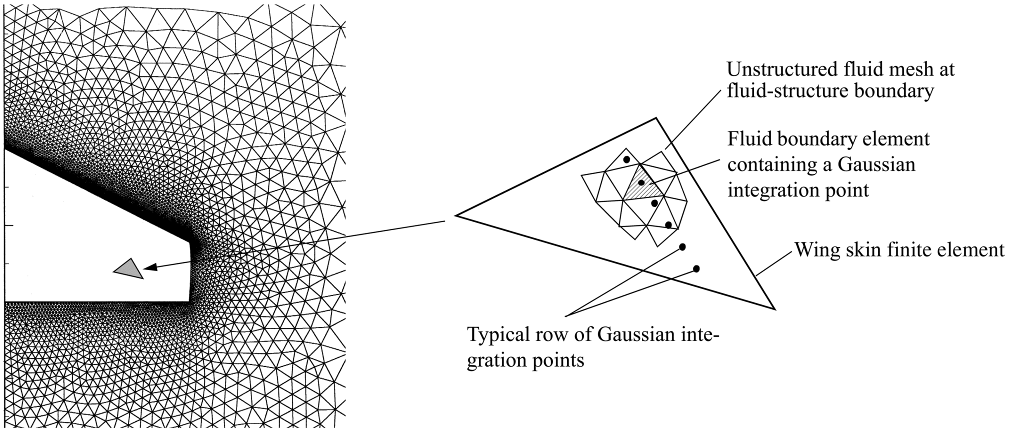

Fig. 5 Direct fluid–structure coupling at the element level (direct Eulerian–Lagrangian approach).

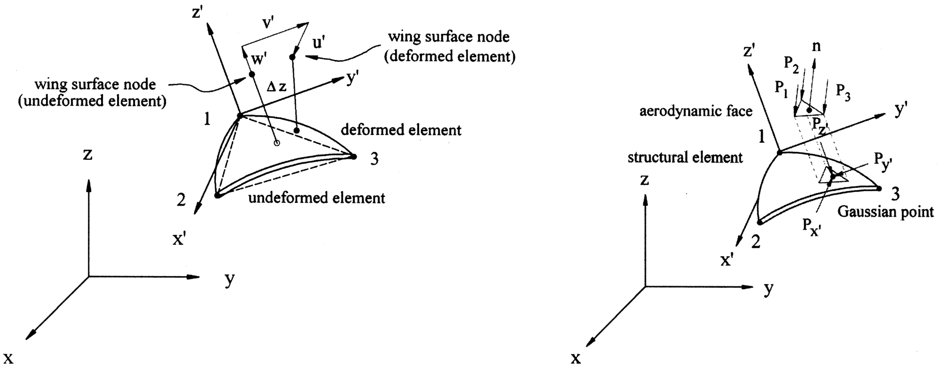

a) b)

Fig. 6 Detail of implementation of direct coupling at the element level: a) mesh motion kinematics in 3-D and b) element-based consistent aerodynamic load calculations.

Table 1 G-wing models: frequencies (in hertz) of the first four natural modes

Model	1B	2B	1T	3B
Linear structure	37.82	132.40	272.51	310.10
Nonlinear structure	37.81	133.30	272.63	310.71
Göttingen wing [8]	37.81	112.85	272.60	241.85

B. Nonlinear Aerodynamic Model

In a modern computational approach, the aerodynamic model is usually expressed in a weak or integral form of the conservation laws:

$$\frac{\partial}{\partial t}\int_{\Omega}\mathbf{W}\,\mathrm{d}V+\int_{\partial\Omega}\mathbf{F}\cdot\mathbf{n}\,\mathrm{d}S=0 \tag{8}$$

where Ω is an element volume with boundary $\partial\Omega$ moving with velocity $\mathbf{U}$, $\mathbf{n}=n_i\mathbf{e}_\mathrm{i}$ is the outward unit normal to $\partial\Omega$, $\mathbf{e}_\mathrm{i}$ are the unit vectors in the x_i directions, and

$$\mathbf{W}=\begin{bmatrix}\rho\\ \rho u_1\\ \rho u_2\\ \rho u_3\\ \rho e\end{bmatrix}\qquad \mathbf{F}_\mathrm{j}=\begin{bmatrix}\rho(u_j-U_j)\\ \rho u_1(u_j-U_j)-\sigma_{1j}\\ \rho u_2(u_j-U_j)-\sigma_{2j}\\ \rho u_3(u_j-U_j)-\sigma_{3j}\\ \rho e(u_j-U_j)-\sigma_{ij}u_i\end{bmatrix} \tag{9}$$

where ρ is the density; $\mathbf{u}$ is the material velocity; e is the total energy per unit mass; u_j and U_j are the Cartesian components of $\mathbf{u}$ and $\mathbf{U}$, respectively; σ_{ij} is the Cartesian stress tensor; and $\mathbf{F}=\mathbf{F}_\mathrm{j}\mathbf{e}_\mathrm{j}$. In the inviscid (Euler) flow model, $\sigma_{ij}=-p\delta_{ij}$, and the equation of state can be used to eliminate the pressure p. A typical Galerkin finite element discretization results in a space-discretized set of nodal equations for the fluid domain of the form [27]

$$\frac{\mathrm{d}}{\mathrm{d}t}\sum_j\mathbf{m}_\mathrm{ij}\mathbf{W}_\mathrm{j}+\mathbf{Q}_\mathrm{i}-\mathbf{D}_\mathrm{i}=0 \tag{10}$$

where $\mathbf{W}_\mathrm{j}$ are the nodal values of $\mathbf{W}$, and the summation on j extends over all nodes in the superelement or control volume associated with node i (i.e., the union of all elements that meet at node i). Here, $\mathbf{m}_\mathrm{ij}$ is the consistent mass matrix, $\mathbf{Q}_i$ is the flux vector, and $\mathbf{D}_\mathrm{i}$ is a vector of dissipative fluxes of the Jameson–Mavriplis type [28,29], as modified in [30,31].

A finite element discretization of the structural domain (wing structure) leads to a similar set of equations, in terms of suitable generalized Lagrangian displacement coordinates $\mathbf{q}_j$:

$$\frac{\mathrm{d}}{\mathrm{d}t}\sum_j\mathbf{m}_{ij}\dot{\mathbf{q}}_j+\mathbf{Q}_\mathrm{i}^\mathrm{E}+\mathbf{Q}_\mathrm{i}^\mathrm{D}-\mathbf{Q}_\mathrm{i}^\mathrm{F}=\mathbf{0} \tag{11}$$

where the sum (assembly) must be carried out over all elements that meet at node i. Here, $\mathbf{Q}_i^E$ are the nonlinear elastic forces, $\mathbf{Q}_i^D$ are the structural damping forces, and $\mathbf{Q}_i^F$ are the consistent generalized fluid forces at the ith node.

A multistage Runge–Kutta scheme is used to integrate the space-discretized system of nonlinear equations forward in time. Time accuracy is maintained by ensuring that the fluid and structural finite element equations are time-marched simultaneously, within the same multistage Runge–Kutta execution loop.

C. Fluid–Structure Coupling

The space-discretized equations for the fluid and structure are coupled through the boundary condition at the fluid–structure boundary, which for the Euler equations is the kinematic boundary condition of tangent flow:

$$\frac{\partial B}{\partial t}+\mathbf{u}\cdot\nabla B=0 \tag{12}$$

where $B(x,y,z,t)=0$ defines the instantaneous locus of the wing surface. To guarantee that the fluid–structure coupling is consistent and does not lead to spurious momentum and energy production at the wing–fluid boundary, it is necessary that the state (position and velocity) of the surface used in the numerical implementation of Eq. (12) is the actual state of the physical wing surface, as defined by the finite element solution. In the direct Eulerian–Lagrangian computational scheme, this is accomplished by working *directly* with the generalized coordinates and associated shape functions for the structural finite elements, and both kinematic (tangent flow) and kinetic (force equilibrium) boundary conditions are imposed at the fluid–structure boundary.

Figure 5 illustrates the concept of direct fluid–structure coupling, as used in the direct Eulerian–Lagrangian computational scheme. The coupling is done at the element level, at the Gaussian integration points for the structural elements. At these points, the exact position and velocity are calculated using the finite element interpolation functions for the structural elements, and the fluid pressures required to calculate the consistent generalized forces are obtained using the corresponding interpolation functions for the fluid elements. In the case of wind-tunnel models of the type used in the G-wing calculations in the next section, the structural model consists of an aluminum alloy plate of the same planform as the wing and covered with lightweight plastic foam or balsa wood to form the airfoil shape, and the surface element displacements and velocities are determined by the method discussed in [27].

Figure 6 further details the element-based approach used in the consistent aerodynamic load calculations. Force vectors are first calculated in the local element coordinate systems using 13-point Gaussian quadrature and then transformed to the global coordinate

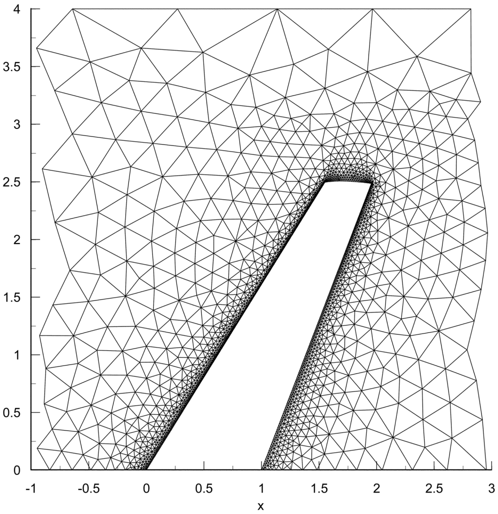

G-Wing

$A = 7.05$
$\Lambda_{LE} = 31.86°$
$\Lambda_{TE} = 21.02°$
$\lambda = 0.4102$

Computational Domain
No. of nodes: 43,344
No. of faces: 430,975
No. of cells: 208,926

No. of structural plate elements: 96
No of structural DOF: 168 (linear)
280 (nonlinear)

Fig. 7 G-wing of a planform similar to the wing studied experimentally in [8].

system as the space-discretized aeroelastic equations are time-marched. The aerodynamic loads are, in a sense, modeled as *follower forces*, resulting in a more accurate prediction of the aeroelastic response. In the aeroelastic calculations using the corresponding *linear* structural model, the aerodynamic loads do not enter the aeroelastic code as follower forces, because only the pressure load in the z direction (normal to the undeformed wing plane) is taken into account.

III. Results and Discussion

A. G-Wing

This wing (Fig. 7) is a generic transport wing of closely similar planform to the wind-tunnel model studied in [8], except that the two small trailing-edge kinks were ignored and a different airfoil section was chosen. An attempt was made to match the first few natural frequencies to the experimental frequencies of the Göttingen wing, by introducing suitable mass and structural taper along the span. In this trial-and-error procedure, more weights were given to matching the first bending (1B) and first torsion (1T) frequencies, because these would be more important in a flutter analysis. No spanwise mass properties were given in [8], and the stated c.g. of the wing and the mass ratios suggest that the (massive) inboard mounting structure must have been included in the wing weight. For this reason, the mass ratios of the wings could not be matched. The frequencies of the first four modes are shown in Table 1 for both the linear and the nonlinear structural models. These differ slightly because of differences in the manner in which the mass and stiffness taper were introduced in the two models; however, the differences are minor and are believed to be unimportant in the aeroelastic calculations. The corresponding frequencies of the Göttingen wing are also given in Table 1. Note that the 1B and 1T frequencies are essentially matched. Finally, it should be mentioned that the third mode of the Göttingen wing is actually an in-plane mode at a frequency slightly above the 2B mode and is not shown in Table 1.

The reason for choosing the 10%-thick ONERA D airfoil was twofold. First, we wanted to see if the transonic LCO behavior observed in the wind-tunnel test was a result of the special nature of the particular supercritical airfoil used or was rather a typical property of a high-aspect-ratio wing with these mass and stiffness properties. Second, we already have substantial experience with the ONERA airfoil in transonic flutter calculations [27].

B. Linear Structure and Nonlinear Aerodynamics

First, a series of transonic flutter calculations were carried out at Mach 0.865 and with a mean lift coefficient in the 0.5–0.6 range, which approximates the experimental conditions at which the Göttingen wing entered a stable LCO, as shown in Fig. 1b. Because of differences in airfoil cambers, this corresponds to an angle of attack of about 4.5 deg for the G-wing with the ONERA airfoil, compared with 2.69 deg for the supercritical Göttingen wing. In addition to trying to match the wing lift coefficient, an attempt was also made to match the mean aeroelastic wing-tip deformations, as well as they could be estimated from Fig. 1b, to ensure that the structural washout effects and geometric nonlinearities were roughly the same in the flutter simulations as in the wind-tunnel tests.

In the calculations, the Mach number was kept fixed and the air density increased until flutter occurred. No LCO-type flutter was observed at the air density of $\rho_a = 0.4177\ \mathrm{kg/m^3}$, corresponding roughly to the wind-tunnel density at which the Göttingen wing exhibited LCO-type flutter, if a mass ratio $\mu = 1000$ is assumed.[§] In fact, the linear G-wing appears stable up through a density of $\rho_a = 1.1\ \mathrm{kg/m^3}$, but limit cycle flutter does eventually appear at an air density of $\rho_a = 1.141\ \mathrm{kg/m^3}$ (see Fig. 8). However, the frequency of this LCO is significantly higher (94 Hz) than that observed in the wind-tunnel test (50.4 Hz), and the corresponding dynamic pressure is 273% higher! In all plots in this paper, wing displacements have been nondimensionalized with respect to the root chord, and wing energy and aerodynamic work have been normalized by the dynamic pressure, to obtain energy/work per unit wing area ($\mathrm{Nm/m^2}$).

C. Nonlinear Structure and Nonlinear Aerodynamics

It is clear from the results of the time-marching flutter calculations using the linear structural model that it is not able to capture the correct LCO behavior of the Göttingen wing, as observed in the wind-tunnel tests. The G-wing model with a linear structure is much too stable at Mach 0.865, and although the effects of transonic aerodynamic nonlinearities do eventually trigger limit cycle flutter, it requires a dynamic pressure of almost 3 times the experimentally observed value. As far as structural nonlinearities arising from large

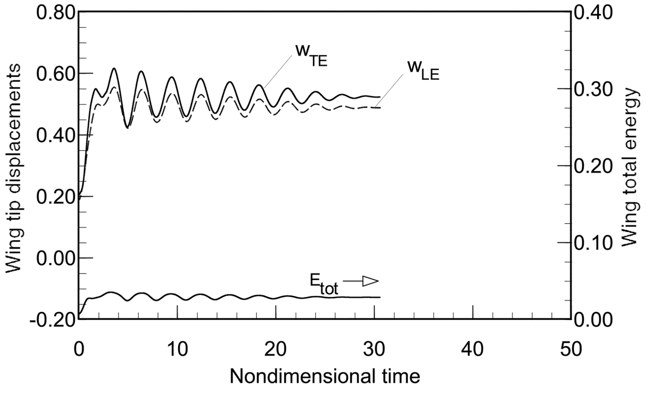

a) $\rho_a = 1.1\ \mathrm{kg/m^3}$

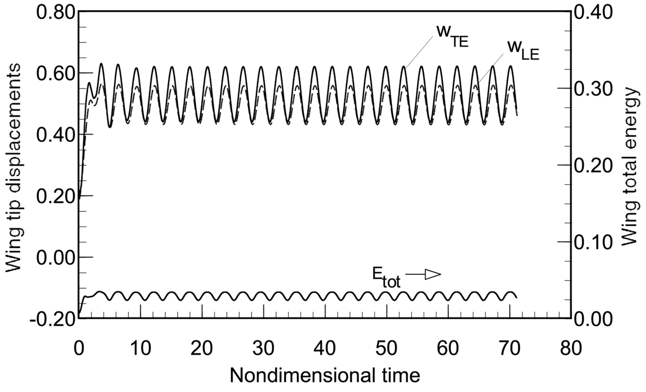

b) $\rho_a = 1.141\ \mathrm{kg/m^3}$

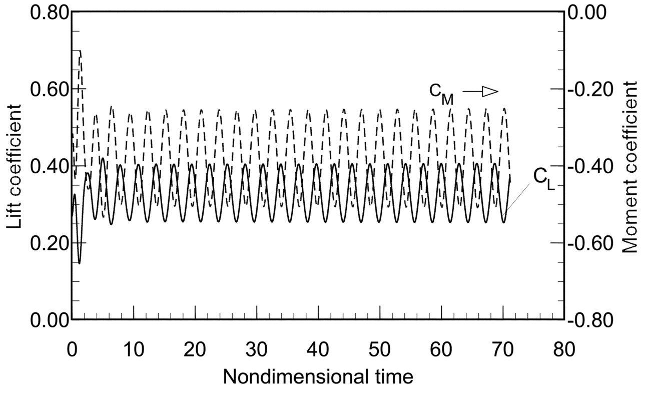

c) Unsteady lift and moment coefficients during LCO, case b

Fig. 8 LCO-type flutter of the G-wing, as calculated using a linear structural model with nonlinear Euler-based aerodynamics. (In all figures, wing-tip displacements are nondimensionalized with respect to wing root chord).

[§] The mass ratio at the test point at which the LCO-type flutter was encountered during wind-tunnel testing was not stated in [8], but can be inferred from Fig. 13 of [8] to fall in the range of 900–1200. Note that the LCO amplitude of the nonlinear G-wing is relatively insensitive to air density in the range of 0.35–0.58 $\mathrm{kg/m^3}$ (Fig. 14), corresponding to mass ratios in the range 720–1200.

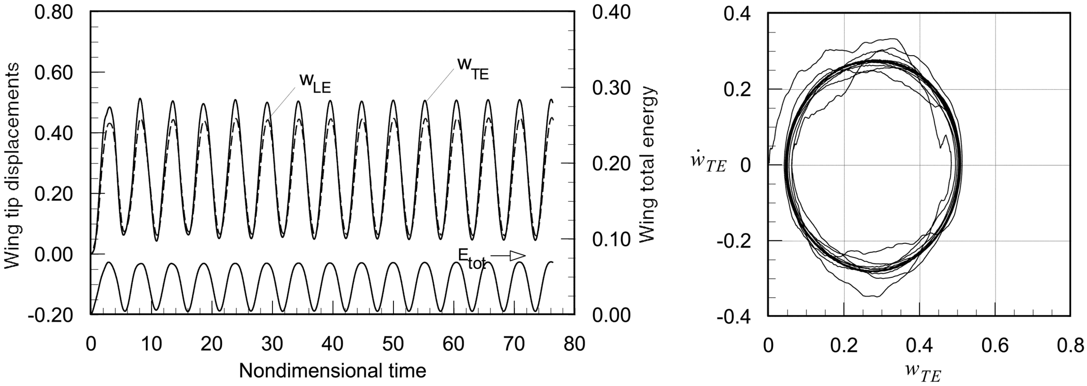

Fig. 9 Limit cycle flutter (LCO) of the G-wing, as predicted by the fully nonlinear aeroelastic model at Mach 0.865 ($\rho_a = 0.4177\ \mathrm{kg/m^3}$).

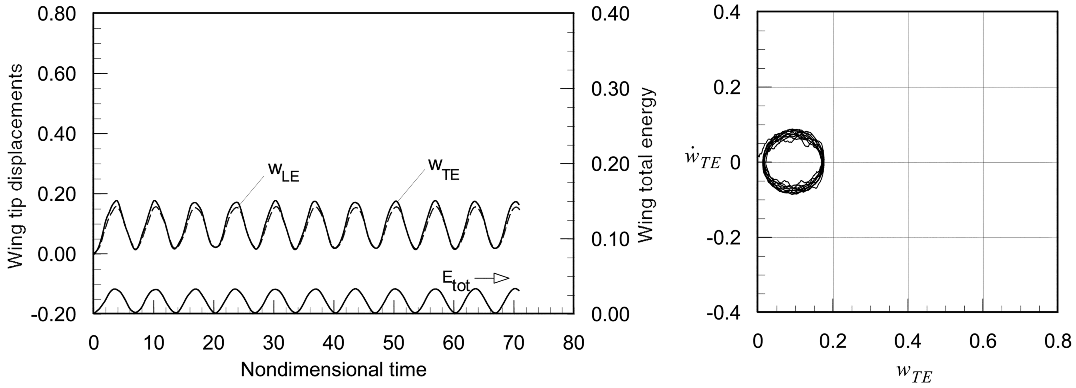

Fig. 10 Effect of reducing density/dynamic pressure to about 23% of the values in Fig. 9, illustrating the persistence of the LCO-type flutter to low dynamic pressures ($M_\infty = 0.865$, $\rho_a = 0.10\ \mathrm{kg/m^3}$).

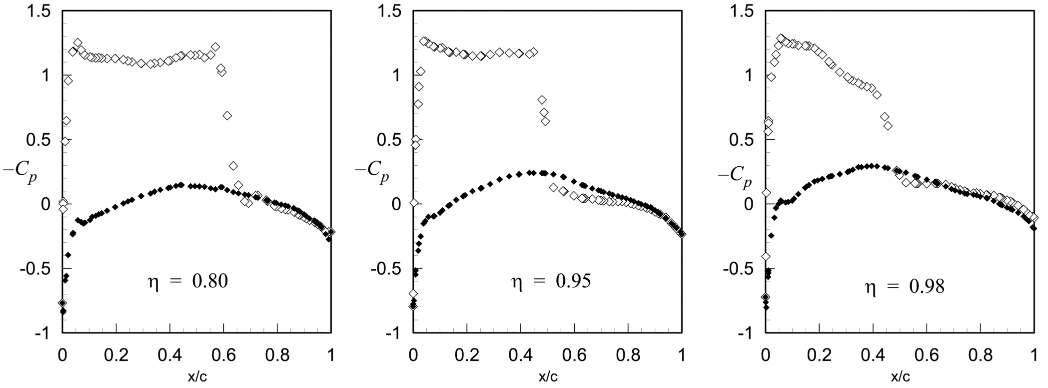

a) Steady flow around a rigid wing

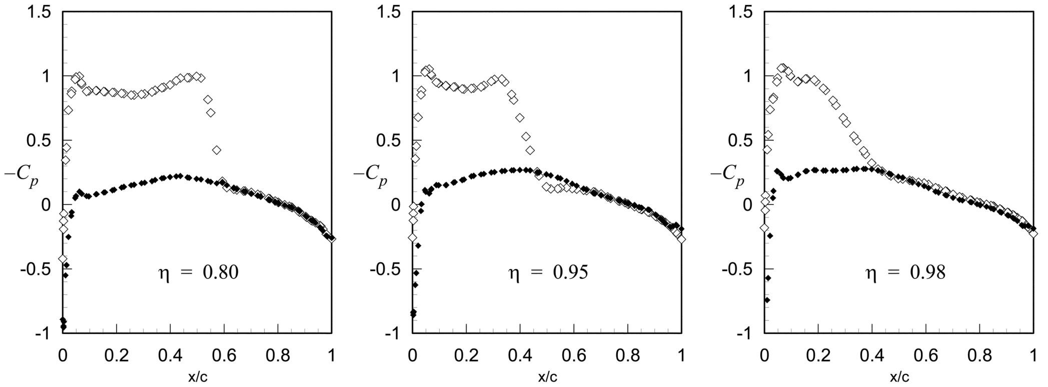

b) Steady flow around a flexible wing (nonlinear structural model)

Fig. 11 Steady pressure distribution about the G-wing at Mach 0.865 and $\alpha = 4.5\ \mathrm{deg}$ ($\rho_a = 0.4177\ \mathrm{kg/m^3}$); open symbols denote the upper surface and solid symbols denote the lower surface.

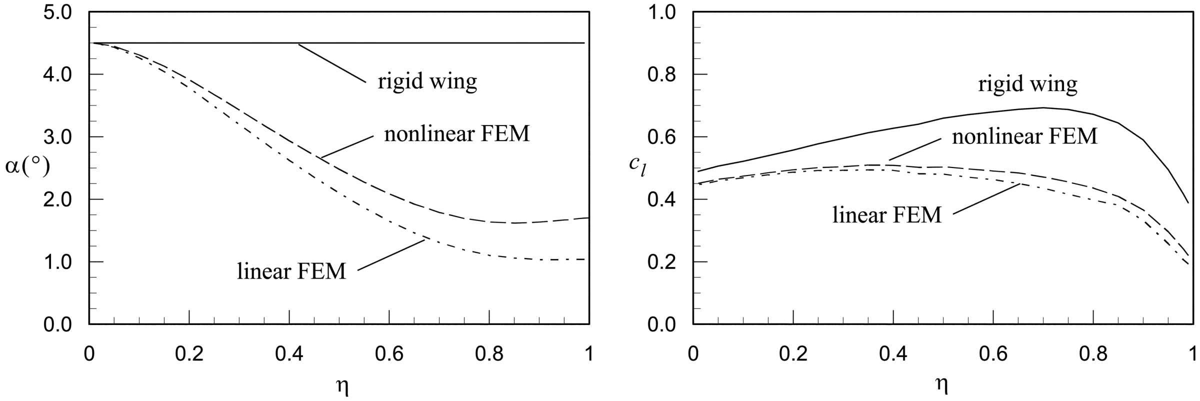

Fig. 12 **Effect of wing deformations on local angle of attack α and local wing-section lift coefficient c_l as a function of relative span location $\eta = y/y_{\text{tip}}$ ($M_\infty = 0.865$; $\alpha = 4.5\,\text{deg}$; $\rho_a = 0.4177\ \text{kg/m}^3$).**

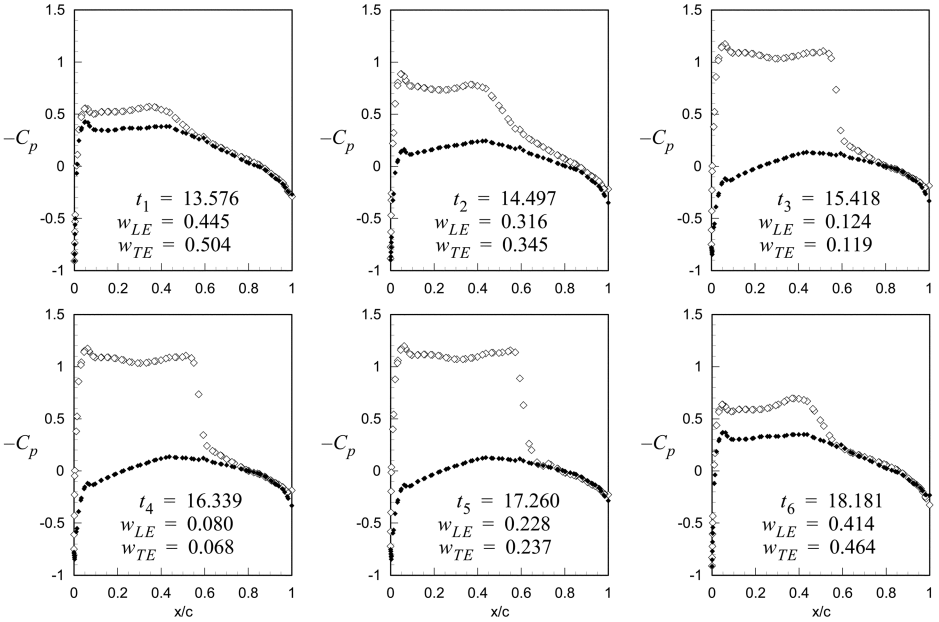

a) At 80% span location

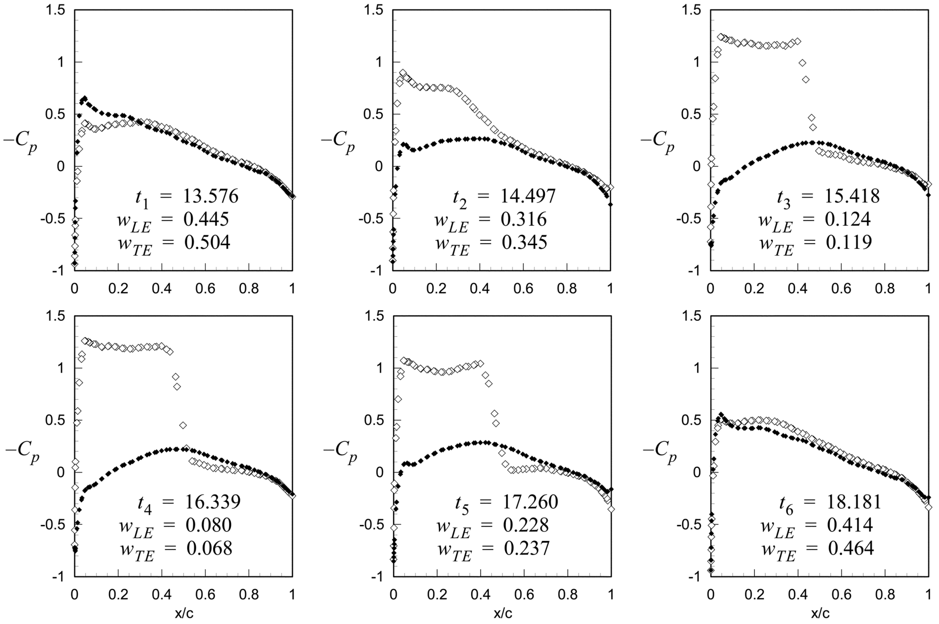

b) At 95% span location

Fig. 13 **Unsteady pressure distribution about the G-wing during LCO flutter at Mach 0.865 and $\alpha = 4.5\,\text{deg}$ ($\rho_a = 0.4177\ \text{kg/m}^3$); open symbols denote the upper surface and solid symbols denote the lower surface.**

deformations are concerned, they ought to be stabilizing, because they typically add nonlinear (cubic) stiffness to the structure. But the calculations using the nonlinear structural model show that the opposite happens.

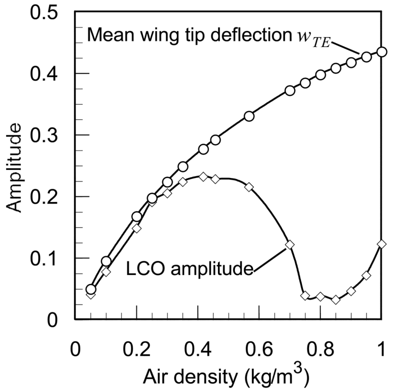

Fig. 14 LCO amplitude and mean wing-tip deflection at the trailing edge vs air density.

The G-wing at transonic Mach numbers represents an example of an inherently nonlinear aeroelastic problem: neither the aerodynamic nor the structural nonlinearities can be ignored, even in a first-order approximation. At an air density of $\rho_a = 0.4177\ \mathrm{kg/m^3}$, corresponding to the wind-tunnel density at which the Göttingen wing exhibited LCO-type flutter, the aeroelastic time-marching calculations reveal a stable LCO (Fig. 9), with a flutter mode very closely resembling the actual mode observed in the wind-tunnel tests (Fig. 1b). The LCO mode shape is essentially the first bending mode of the wing, modified somewhat by aeroelastic effects, with each streamwise wing section executing a motion very closely resembling a SDOF pitching about an axis upstream of the leading edge (nose-down flutter mode). The predicted flutter frequency is 52.4 Hz, which is very close (+4%) to the LCO frequency of 50.4 Hz observed in the wind-tunnel tests. The predicted amplitudes are significantly higher, however, but it should be kept in mind that the G-wing has a different airfoil and the effect of structural damping has been neglected.

Because of strong interactions between the aeroelastic washout and the emerging flutter mode, limit cycle flutter can be observed over a wide range of dynamic pressures in the present nonlinear time-marching flutter simulations. At Mach 0.865, the LCO-type

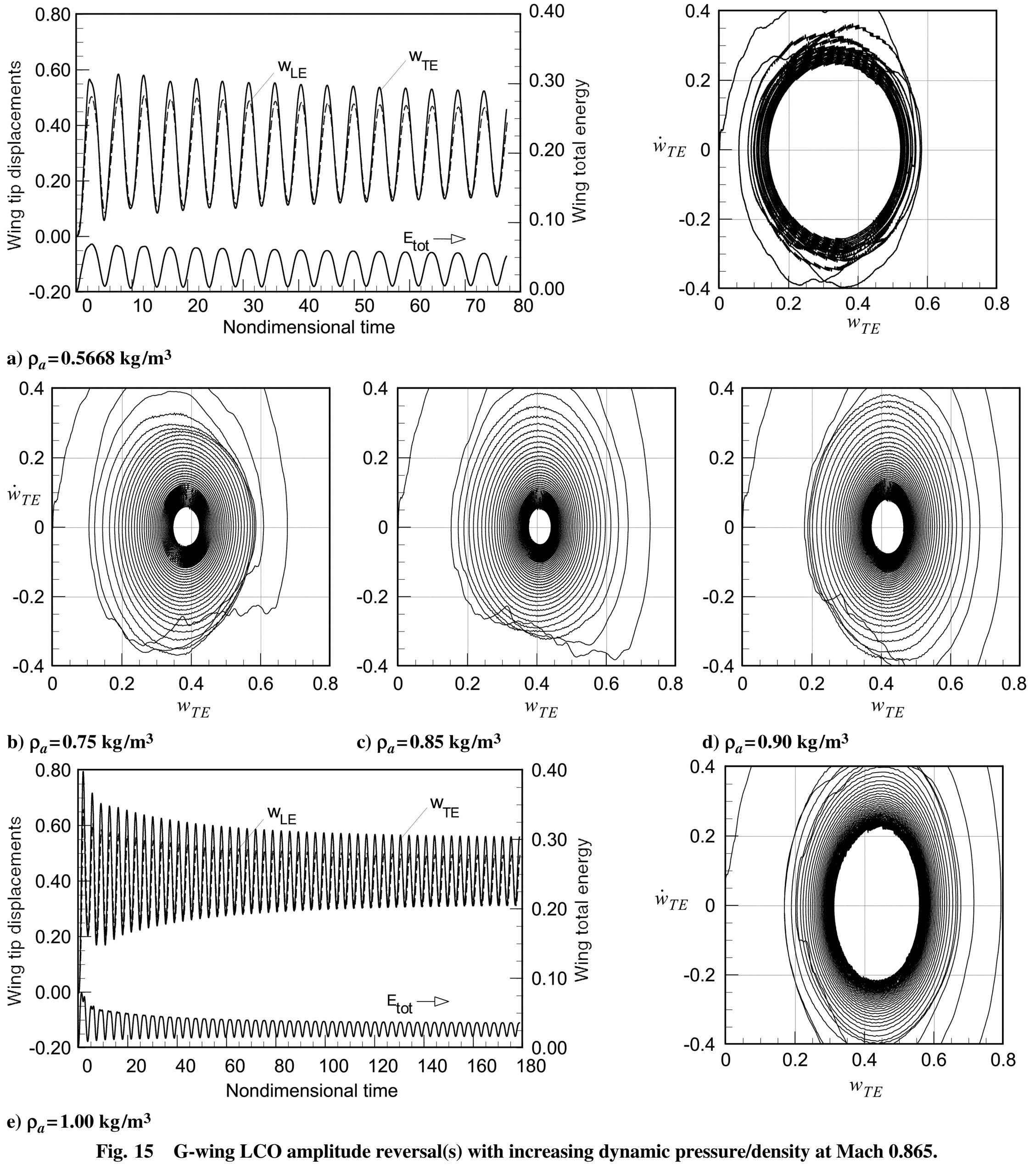

a) $\rho_a = 0.5668\ \mathrm{kg/m^3}$

b) $\rho_a = 0.75\ \mathrm{kg/m^3}$

c) $\rho_a = 0.85\ \mathrm{kg/m^3}$

d) $\rho_a = 0.90\ \mathrm{kg/m^3}$

e) $\rho_a = 1.00\ \mathrm{kg/m^3}$

Fig. 15 G-wing LCO amplitude reversal(s) with increasing dynamic pressure/density at Mach 0.865.

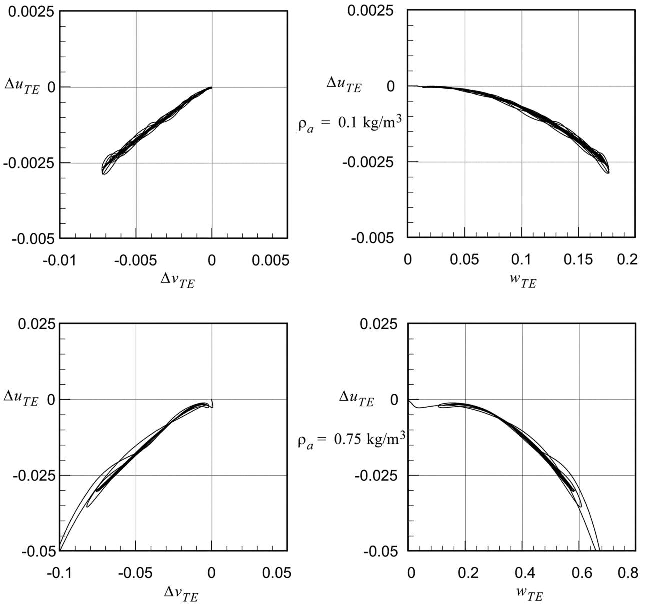

Fig. 16 Representative phase plots for the in-plane wing-tip displacements and comparisons with w_{TE}.

flutter of the G-wing persists down to very low dynamic pressures (or densities), as shown in Fig. 10, which corresponds to $\rho_a = 0.10\ \mathrm{kg/m^3}$: less that one-fourth of the density in Fig. 9. Additional calculations for $\rho_a = 0.05\ \mathrm{kg/m^3}$ (not shown) reveal that the LCO is still there, albeit with a smaller (but stable) amplitude.

Our calculations indicate that the aeroelastic washout effect is strongly stabilizing at transonic Mach numbers, because the aeroelastic untwist unloads the critical tip region of the wing, resulting in weaker and more forward part-chord shocks. Both of these effects are stabilizing from a flutter standpoint, because they lead to an earlier transition from Tijdeman type A (continuous) to type B (intermittent) shock motion, which is known to decrease the rate of aerodynamic work on the wing, resulting in LCO-type flutter [20]. These two phenomena are illustrated in Figs. 11–13. Figure 11 compares the steady pressure coefficient at 3 span locations on the outboard region of the wing, calculated assuming a rigid wing (Fig. 11a) and a flexible wing (Fig. 11b), corresponding to the operating conditions listed in Fig. 9. Note that the wing deformations cause a significant reduction in the aerodynamic loading on the outboard region of the wing, resulting in a weakening and forward shift of the upper-surface shock. At the same time, the peak Mach numbers (not shown) in the supersonic region are reduced significantly at all outboard span locations. From Fig. 12, which shows the corresponding local angle of attack and local wing-section lift coefficient, it is apparent that this "load relief" arises from the structural washout effect. Figure 13 shows the instantaneous pressure distribution on the upper and lower wing surfaces at 6 different times during a typical LCO cycle, beginning at a point of maximum wing-tip deflection, with each snapshot being roughly 65 deg advanced in temporal phase from the previous one. From these plots, it can be seen that type B (intermittent) shock motion has been established at the 95% span location and is very close to intermittent at the 80% span location.

For wings of flexibility representative of the G-wing, the LCO amplitude is not a monotonic function of the dynamic pressure, and for at least a range of pressures and densities, the LCO amplitudes actually decrease with increasing dynamic pressure or air density at a given Mach number and reduced velocity. This phenomenon is revealed in the results shown in Figs. 14 and 15. In such cases, *decreasing* the dynamic pressure will *increase* the LCO amplitude over the corresponding range of pressures in which "LCO amplitude reversal" occurs, as shown in Fig. 14. Also shown in Fig. 14 is the mean tip deflection at the trailing edge of the wing as a function of air density.

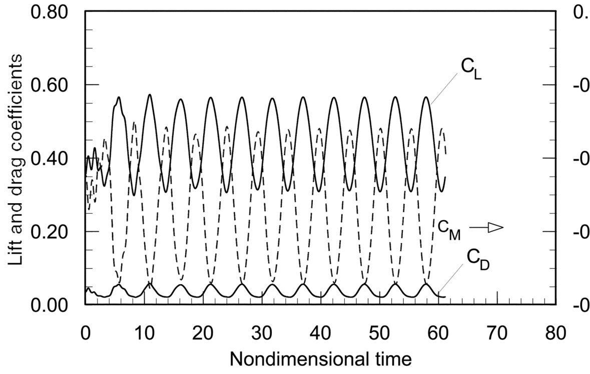

a) $\rho_a = 0.4177\ \mathrm{kg/m^3}$

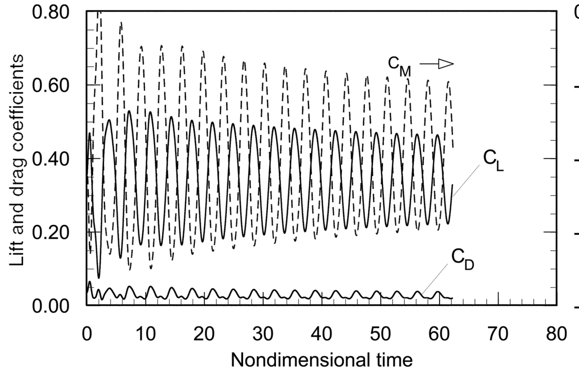

b) $\rho_a = 1.00\ \mathrm{kg/m^3}$

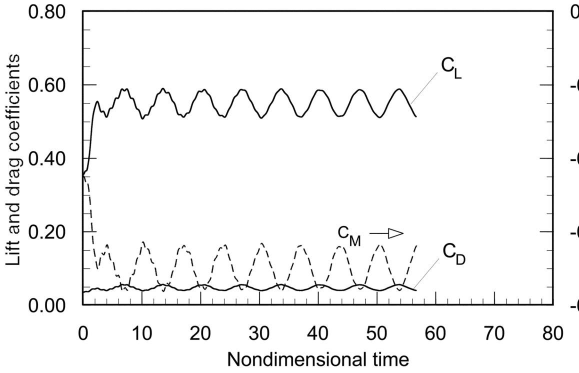

c) $\rho_a = 0.10\ \mathrm{kg/m^3}$

Fig. 17 Wing lift, moment, and drag coefficients vs time, during LCO-type flutter of the G-wing at Mach 0.865.

Representative phase plots of the in-plane wing displacements Δu_{TE} and Δv_{TE} in the chordwise and spanwise directions, respectively, at the wing-tip trailing edge are shown in Fig. 16.¶ To what degree the in-plane degrees of freedom (which are present in the nonlinear structural model only) affect the flutter stability of the wing, and transonic limit cycle flutter in particular, is still being studied and no definite conclusions have been reached to date. Although the observed lead-lag amplitudes are relatively small, of the order of a few percent of chord, this in-plane motion may still be destabilizing if it allows the wing to extract additional net positive energy from the airstream over each limit cycle oscillation.

Finally, Fig. 17 shows representative plots of the predicted lift, moment, and drag coefficients vs time during LCO-type flutter of the G-wing at Mach 0.865. As pointed out in [8], the oscillation amplitudes of the lift and moment coefficients are very substantial

---

¶In [32], the Δu_{TE} and Δv_{TE} labels on the axes of Fig. 13 were accidentally switched.

and would be expected to have a significant effect on the longitudinal motion and stability of the airplane.

D. Practical Implications

The results show that for high-aspect-ratio swept wings of the class represented by the Göttingen wing, transonic LCO-type flutter persists down to very low dynamic pressures if the flight Mach number is held constant at values typical of the Göttingen wing ($M_\infty = 0.865$). Furthermore, for wings of representative flexibility, Figs. 14 and 15 show that the aeroelastic washout effect can have a very counterintuitive result, in that *increasing the dynamic pressure may actually be stabilizing*, in the sense that it decreases the LCO amplitudes at a given Mach number. Conversely, *decreasing* the dynamic pressure may *increase* the LCO amplitude. This surprising behavior suggests that transonic flutter at high altitudes may become possible, even if the wing is stable at lower flight altitudes. It is also of relevance in wind-tunnel testing, and the use of bypass or blowout valves to rapidly drop the tunnel dynamic pressure (or density) when flutter is encountered may not be as effective as is generally expected for this class of wings.

IV. Conclusions

1) The aeroelastic mechanism responsible for the observed limit cycle flutter of the Göttingen wing and the G-wing studied in this paper appears to be fundamentally different from the corresponding mechanism(s) responsible for the LCO-type flutter of low-aspect-ratio wings, as observed on the F-16 aircraft, for example.

2) In the case of a high-aspect-ratio swept wing, the structural washout effect from aeroelastic deformations plays a fundamental role in throttling the energy flow from the airstream to the wing, resulting in limit cycle flutter. This mechanism is strong enough to explain the low-amplitude LCOs observed in the Göttingen wing, even in the absence of flow separation.

3) The resulting transonic limit cycle flutter mode has bending and torsion almost perfectly in phase at any given span location, and the 2-D streamwise wing-section motion resembles a SDOF pitching mode with an axis of rotation forward of the leading edge.

4) In the swept-wing case, the apparent pitching motion of the streamwise wing sections arises naturally through the structural washout effect and is present in the first bending mode that enters LCO flutter.

5) Because of strong interactions between the aeroelastic washout and the flutter mode, limit cycle flutter can be observed over a wide range of dynamic pressures at any given Mach number near the transonic dip.

6) For swept wings of sufficient flexibility, the aeroelastic washout effect can produce the counterintuitive result that increasing the dynamic pressure may be stabilizing, in the sense that it decreases the LCO amplitude at a given transonic Mach number. Conversely, *decreasing* the dynamic pressure may increase the LCO flutter amplitude: a conclusion of obvious relevance to wind-tunnel and flight testing.

7) A nonlinear structural model was necessary to capture the observed LCO flutter behavior of the Göttingen wing. If a linear structural model is used, the critical dynamic pressure at LCO flutter onset is overpredicted by a factor of nearly 3, and the predicted flutter mode is at a frequency much higher than was observed during wind-tunnel tests.

Acknowledgment

This research was supported by NASA grant NCC 4-157.

References

[1] Bendiksen, O. O., "Energy Approach to Flutter Suppression and Aeroelastic Control," *Journal of Guidance, Control, and Dynamics*, Vol. 24, No. 1, Jan.–Feb. 2001, pp. 176–184.

[2] Cunningham, A. M., Jr., "Buzz, Buffet, and LCO on Military Aircraft: The Aeroelastician's Nightmare," *Proceedings of the International Forum on Structural Dynamics and Aeroelasticity 2003* [CD-ROM], Netherlands Association of Aeronautical Engineers, Amsterdam, 4–6 June 2003.

[3] Bendiksen, O. O., "Nonclassical Aileron Buzz in Transonic Flow," AIAA/ASME/ASCE/AHS/ASC 34th Structures, Structural Dynamics and Materials Conference, La Jolla, CA, AIAA Paper 93-1479, Apr. 1993.

[4] Bendiksen, O. O., "Transonic Flutter," AIAA/ASME/ASCE/AHS/ASC 43rd SDM Conference, Denver, CO, AIAA Paper 2002-1488, Apr. 2002.

[5] Knipfer, A., and Schewe, G., "Investigation of an Oscillating Supercritical 2-D Wing Section in a Transonic Flow," AIAA Paper 99-0653, Jan. 1999.

[6] Schewe, G., Knipfer, A., Mai, H., and Dietz, G., "Experimental and Numerical Investigation of Nonlinear Effects in Transonic Flutter," DLR, German Aerospace Center, Paper DLR IB 232-2002 J 01, 2002.

[7] Schewe, G., Mai, H., and Dietz, G., "Nonlinear Effects in Transonic Flutter with Emphasis on Manifestations of Limit Cycle Oscillations," *Journal of Fluids and Structures*, Vol. 18, No. 1, 2003, pp. 3–22. doi:10.1016/S0889-9746(03)00085-9

[8] Dietz, G., Schewe, G., Kiessling, F., and Sinapius, M., "Limit-Cycle-Oscillation Experiments at a Transport Aircraft Wing Model," *Proceedings of the International Forum on Structural Dynamics and Aeroelasticity 2003* [CD-ROM], Netherlands Association of Aeronautical Engineers, Amsterdam, 4–6 June 2003.

[9] Eckstrom, C. V., Seidel, D. A., and Sanford, M. C., "Measurements of Unsteady Pressure and Structural Response for an Elastic Supercritical Wing," NASA TP 3443, November 1994.

[10] Gránásy, P., Matsushita, H., and Saitoh, K., "Nonlinear Aeroelastic Phenomena at Transonic Region," *Proceedings of the International Forum on Aeroelasticity and Structural Dynamics*, Vol. 3, Esagrafica, Rome, 17–20 June 1997, pp. 379–385.

[11] Edwards, J. W., Schuster, D.M., Keller, D.F., and Moses, R.W., "MAVRIC Flutter Model Transonic Limit Cycle Oscillation Test," NASA TM-2001-210877, May 2001.

[12] Bendiksen, O. O., and Kousen, K. A., "Transonic Flutter Analysis Using the Euler Equations," AIAA Dynamics Specialists Conference, Monterey, CA, AIAA Paper 87-0911, Apr. 1987.

[13] Kousen, K. A., and Bendiksen, O. O., "Nonlinear Aspects of the Transonic Aeroelastic Stability Problem," AIAA/ASME/ASCE/AHS 29th Structures, Structural Dynamics and Materials Conference, Williamsburg, VA, AIAA Paper 88-2306, Apr. 1988, pp. 760–769.

[14] Bendiksen, O. O., "A New Approach to Computational Aeroelasticity," 32nd AIAA/ASME/ASCE/AHS/ASC Structures, Structural Dynamics and Materials Conference, Baltimore, MD, AIAA, Washington, D.C., 8–10 Apr. 1991, pp. 1712–1727.

[15] Kousen, K. A., and Bendiksen, O. O., "Limit Cycle Phenomena in Computational Transonic Aeroelasticity," *Journal of Aircraft*, Vol. 31, Nov.–Dec. 1994, pp. 1257–1263. doi:10.2514/3.46644

[16] Thomas, J. P., Dowell, E. H., and Hall, K. C., "Modeling Viscous Transonic Limit Cycle Oscillation Behavior Using a Harmonic Balance Approach," *Journal of Aircraft*, Vol. 41, No. 6, 2004, pp. 1266–1274. doi:10.2514/1.9839

[17] Weber, S., Jones, K. D., Ekaterinaris, J. A., and Platzer, M. F., "Transonic Flutter Computations for a 2-D Supercritical Wing," 36th Aerospace Sciences Meeting and Exhibit, Reno, NV, AIAA Paper 99-0798, Jan. 1999.

[18] Tang, L., Bartels, R. E., Chen, P. C., and Liu, D. D., "Simulation of Transonic Limit Cycle Oscillations Using a CFD Time-Marching Method," AIAA/ASME/ASCE/AHS/ASC 42nd Structures, Structural Dynamics and Materials Conference, Seattle, WA, AIAA Paper 2001-1290, Apr. 2001.

[19] Pranata, B. B., Kok, J. C., Spekreijse, S. P., Hounjet, M. H. L., and Meijer, J. J., "Simulation of Limit Cycle Oscillation of Fighter Aircraft at Moderate Angle of Attack," *Proceedings of the International Forum on Structural Dynamics and Aeroelasticity 2003*, Amsterdam, 4–6 June 2003.

[20] Bendiksen, O. O., "Transonic Limit Cycle Flutter/LCO," AIAA/ASME/ASCE/AHS/ASC 45th Structures, Structural Dynamics and Materials Conference, Palm Springs, CA, AIAA Paper 2004-1694, Apr. 2004.

[21] Dietz, G., Schewe, G., and Mai, H., "Amplification and Amplitude Limitation on Heave/Pitch Limit-Cycle Oscillations Close to the Transonic Dip," *Journal of Fluids and Structures*, Vol. 22, No. 4, 2006, pp. 505–527. doi:10.1016/j.jfluidstructs.2006.01.004

[22] Thomas, J. P., Dowell, E. H., Hall, K. C., and Denegri, C. M., "Further Investigation of Modeling Limit Cycle Oscillation Behavior of the F-16

Using a Harmonic Balance Approach," 46th AIAA/ASME/ASCE/AHS/ASC Structures, Structural Dynamics, and Materials Conference, Austin, TX, AIAA Paper 2005-1917, Apr. 2005.

[23] Bendiksen, O. O., "Effect of Wing Deformations and Sweep on Transonic Limit Cycle Flutter of Flexible Wings," International Forum on Structural Dynamics and Aeroelasticity 2007, Stockholm, Confederation of European Aerospace Societies Paper IF-031, June 2007.

[24] Seber, G., and Bendiksen, O. O., "Nonlinear Flutter Calculations Using Finite Elements in a Direct Eulerian–Lagrangian Formulation," *AIAA Journal*, Vol. 46, No. 6, 2008, pp. 1331–1341.
doi:10.2514/1.27844; also AIAA Paper 2005-1856, Apr. 2005.

[25] Batoz, J. L., and Lardeur, P., "A Discrete Shear Triangular Nine D. O. F. Element for Analysis of Thick to Very Thin Plates," *International Journal for Numerical Methods in Engineering*, Vol. 28, No. 3, 1989, pp. 533–560.
doi:10.1002/nme.1620280305

[26] Patel, S., "A Discrete Shear Triangular Finite Element with Applications to the Vibration Analysis of Thin and Thick Plates," M.S. Thesis, Dept. of Mechanical and Aerospace Engineering, Univ. of California, Los Angeles, Los Angeles, 1995.

[27] Bendiksen, O. O., "Modern Developments in Computational Aeroelasticity," *Proceedings of the Institution of Mechanical Engineers. Part G, Journal of Aerospace Engineering*, Vol. 218, No. 3, June 2004, pp. 157–178.
doi:10.1243/0954410041872861

[28] Jameson, A., and Mavriplis, D. J., "Finite Volume Solution of the Two-Dimensional Euler Equations on a Regular Triangular Mesh," AIAA Paper 85-0435, Jan. 1985.

[29] Mavriplis, D. J., "Accurate Multigrid Solution of the Euler Equations on Unstructured and Adaptive Meshes," *AIAA Journal*, Vol. 28, Feb. 1990, pp. 213–221.
doi:10.2514/3.10377

[30] Davis, G. A., and Bendiksen, O. O., "Unsteady Transonic Two-Dimensional Euler Solutions Using Finite Elements," *AIAA Journal*, Vol. 31, June 1993, pp. 1051–1059.
doi:10.2514/3.11728

[31] Hwang, G., "Parallel Finite Element Solutions of Nonlinear Aeroelastic and Aeroservoelastic Problems in Three-Dimensional Transonic Flows," Ph.D. Dissertation, Dept. of Mechanical and Aerospace Engineering, Univ. of California, Los Angeles, Los Angeles, Mar. 1997.

[32] Bendiksen, O. O., "Transonic Limit Cycle Flutter of High-Aspect-Ratio Swept Wings," 47th AIAA/ASME/ASCE/AHS/ASC Structures, Structural Dynamics and Materials Conference, Newport, RI, AIAA Paper 2006-1635, May 2006.